

Emergence of Stable Meron Quartets in Twisted Magnets

Kyoung-Min Kim,* Gyungchoon Go, Moon Jip Park, and Se Kwon Kim*



Cite This: *Nano Lett.* 2024, 24, 74–81



Read Online

ACCESS |

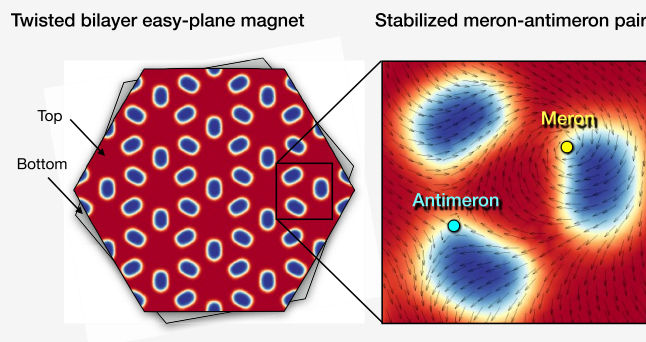
Metrics & More

Article Recommendations

Supporting Information

ABSTRACT: The investigation of twist engineering in easy-axis magnetic systems has revealed remarkable potential for generating topological spin textures. Implementing twist engineering in easy-plane magnets, we introduce a novel approach to achieving fractional topological spin textures, such as merons. Through atomistic spin simulations on twisted bilayer magnets, we demonstrate the formation of a stable double Meron pair, which we refer to as the “Meron Quartet” (MQ). Unlike a single pair, the merons within the MQ exhibit exceptional stability against pair annihilation due to the protective localization mechanism induced by the twist that prevents collision of the Meron cores. Furthermore, we showcase that the stability of the MQ can be enhanced by adjusting the twist angle, resulting in an increased resistance to external perturbations such as external magnetic fields. Our findings highlight the twisted magnet as a promising platform for achieving merons as stable magnetic quasiparticles in van der Waals magnets.

KEYWORDS: merons, magnetic vortices, topological spin textures, twist engineering, van der Waals magnets, moiré magnets



The search for novel spin configurations motivated by fundamental interest and technological applications has led to the discovery of intriguing textures with nontrivial topology in various magnetic systems.¹ Specifically, vortex-type topological spin textures, so-called merons, have been observed in confined magnetic disks^{2–6} and continuous thin films.^{7–13} Recently, monolayer chromium trichloride (CrCl₃), a two-dimensional (2D) van der Waals (vdW) magnetic crystal, has emerged as a promising candidate for achieving merons in this novel atomically thin limit.^{14–16} The intrinsic easy-plane magnetic anisotropy in such a system offers a pathway to attaining in-plane swirling spin textures for merons. However, these merons are inherently unstable against pair annihilation and possess only a limited lifespan.¹⁶ The mechanism responsible for stabilizing such merons has yet to be definitively determined, hampering future exploration of merons in 2D vdW magnets.

The field of twist engineering has opened up a fascinating realm of possibilities in generating topological spin textures in 2D vdW magnets. By harnessing moiré patterns, researchers have demonstrated the creation of skyrmion spin textures in lattice-mismatched heterostructures^{17–19} and twisted homobilayer systems,^{20–25} with a primary focus on Ising-type easy-axis magnetic systems. However, extending this approach to XY-type easy-plane magnets holds tremendous intrigue, as it enables exploration of captivating phenomena such as the Berezinskii–Kosterlitz–Thouless transition,^{26,27} the emergence of merons,^{15,16} and the potential discovery of hidden magnetic phases driven by strong spin fluctuations.²⁸ The

recent discovery of twisted magnets further enhances the allure, prompting a continued investigation into the captivating moiré effects in these systems.^{29–32}

In this study, we investigate twist engineering in vdW magnets as a promising avenue to realize stable merons. By conducting atomistic spin simulations, we demonstrate that antiferromagnetic domain arrays in the twisted magnet^{23,24,29–34} can be utilized to localize the cores of merons along the boundaries of their respective domains (Figure 1a–b). This localization mechanism effectively preserves the stable spin configuration of the Meron pair by separating their cores (Figure 1c). Furthermore, we show that the stability of the merons can be tuned by adjusting the twist angle, providing controllable resistance against external magnetic fields. These findings present a promising avenue for achieving stable merons as magnetic quasiparticles in vdW magnets, offering the opportunity to explore their captivating properties with significant flexibility through external stimuli^{35,36} or the creation of heterostructures.³⁷

We constructed twisted bilayer magnets by rotating two magnetic layers in a honeycomb lattice with a relative twist

Received: August 27, 2023

Revised: December 21, 2023

Accepted: December 22, 2023

Published: December 26, 2023



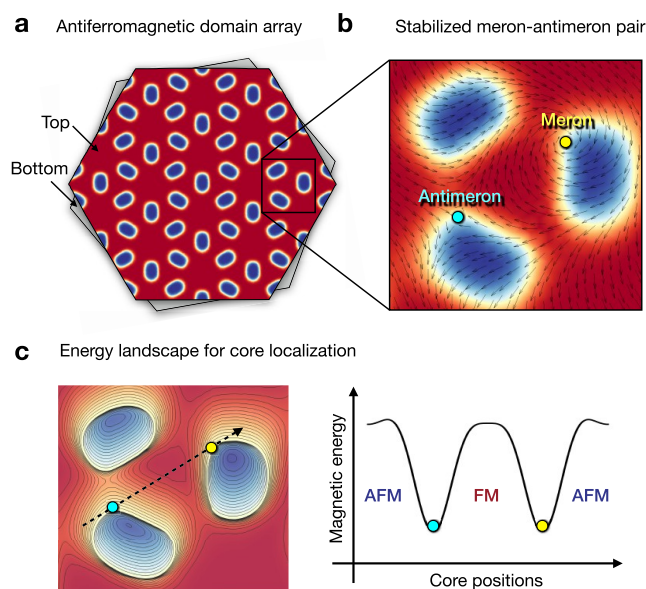


Figure 1. Schematic illustration of a stable meron-antimeron pair in a twisted magnet. a: Twist-induced antiferromagnetic (AFM) domain array in a ferromagnetic (FM) order background. Red and blue indicate parallel and antiparallel spin alignments between the top and bottom layers, respectively. b: Emergence of a stable Meron-antimeron pair. Arrows and circles depict their in-plane winding textures and core positions, respectively. c: Schematic energy landscape for localizing the cores within different AFM domains (left) and its schematic profile along the dashed line (right).

angle (Figure 2a). These twisted magnets can be effectively described using a Heisenberg spin model given by²⁴

$$H = -\frac{J}{2} \sum_{l=t,b} \sum_{\langle i,j \rangle} \mathbf{S}_i^l \cdot \mathbf{S}_j^l + A \sum_{l=t,b} \sum_i (\mathbf{S}_i^l \cdot \hat{\mathbf{z}})^2 + \sum_{i,j} J_{ij}^\perp \mathbf{S}_i^t \cdot \mathbf{S}_j^b \quad (1)$$

Here, \mathbf{S}_i^l represents the spin at site i on the top layer ($l = t$) and the bottom layer ($l = b$). J represents the intralayer FM exchange interactions between nearest-neighbor spins. $A = 0.1$ meV represents the single-ion anisotropy energy favoring in-plane magnetization. J_{ij}^\perp represent the interlayer exchange interactions, which are adopted from previous ab initio calculations on bilayer CrI_3 .²⁴ Due to so-called stacking-dependent interlayer magnetism,^{21,39–43} J_{ij}^\perp switch from FM to AFM coupling depending on the local stacking pattern between the two magnetic layers (see Supporting Information (SI)³⁸). Consequently, the interlayer exchange coupling exhibits the coexistence of AFM and FM interactions in the moiré superlattice accommodating various local stacking patterns (Figure 2a).^{20–25,34} We illustrate this behavior in Figure 2b through the map of the local interlayer exchange energy $J_i^\perp = \sum_j J_{ij}^\perp$ computed in an FM configuration $\mathbf{S}_i = S\hat{\mathbf{z}}$.^{20,22,24,34} Specifically, in the monoclinic stacking region (red patches), J_i^\perp exhibits AFM character ($J_i^\perp > 0$), indicating a tendency for the spins in the top and bottom layers to align antiparallel to each other. Conversely, in the other stacking regions, J_i^\perp exhibits FM character ($J_i^\perp < 0$), signifying a preference for parallel alignment. As a result, the twisted magnet embeds local AFM patches in the background of FM coupling (Figure 2b). This spin model can be applied to CrI_3 by adapting its intrinsic easy-axis magnetic anisotropy into

easy-plane magnetic anisotropy through external stimuli such as strain, gate voltage, or surface adsorption.^{44–48}

In this work, we investigate the influence of the AFM patches on the stabilization of merons. We first identify the magnetic phases of the twisted easy-plane magnets. Our atomistic simulations on eq 1, conducted using an iterative optimization method (see SI³⁸), reveal the zero-temperature magnetic phase diagram shown in Figure 2c. Within this diagram, we observe two distinct magnetic phases: an FM phase and a magnetic domain (MD) phase. The FM phase exhibits a uniform spin configuration with a parallel alignment between the spins of the top and bottom layers. On the other hand, the MD phase exhibits antiparallel alignment within the AFM patches, while maintaining parallel alignment outside these patches to minimize the interlayer exchange energy (Figure 2d–f). This contrasting AFM-FM order results in the formation of AFM domains within each AFM patch as well as domain walls surrounding the domains, characterized by spin rotations of 90° and -90° . Furthermore, the AFM domains are arranged into an array structure across the superlattice, resembling a Kagome lattice. We dub this distinctive magnetic structure an AFM domain array.

We attribute the emergence of the AFM domain array to the amplified effect of interlayer exchange in the small twist angle regime ($\theta < \theta_{c1} \sim \sqrt{J_\perp/J}$). In this regime, the formation of an AFM domain becomes energetically favorable as the reduction in the interlayer exchange energy ($\Delta E_{\text{inter}} \sim -J_\perp \frac{L^2}{a^2} \sim -J_\perp \theta^{-2}$) outweighs the increase in the intralayer exchange energy ($\Delta E_{\text{intra}} \sim J$). Here, we consider J_\perp as the average value of J_{ij}^\perp within the AFM patch. The patch is approximated as a disk with a radius denoted by $L \sim a/\theta$, where a represents the lattice constant of the honeycomb lattice. Despite interlayer exchange being weaker than intralayer exchange, its effect is significantly amplified by the large size of the AFM patch (πL^2). Consequently, the formation of the AFM domain array is expected when the twist angle is sufficiently small. This phenomenon manifests in the phase diagram, which exhibits a consistent relationship $\theta_{c1} \sim \sqrt{J_\perp/J}$ for the phase boundary between the FM and MD phases (dashed line in Figure 2c).

A Meron is a vortexlike topological spin texture, characterized by an integer winding number. In contrast to conventional magnetic vortices, the core of a Meron exhibits an out-of-plane polarization, resulting in a unique half-skyrmion number denoted as¹²

$$Q = \frac{1}{4\pi} \int dx \int dy (\partial_x \mathbf{n} \times \partial_y \mathbf{n}) \cdot \mathbf{n} = p \cdot w = -\frac{1}{2} \quad (2)$$

Here, the vector field $\mathbf{n} = (\sin \vartheta \cos \varphi, \sin \vartheta \sin \varphi, \cos \vartheta)$ represents the orientation of spins. The polarity p and vorticity w of \mathbf{n} are defined by $p = 1/2[\cos \vartheta(r = \infty) - \cos \vartheta(r = 0)]$ and $w = 1/2\pi \oint_\gamma d\mathbf{l} \cdot \nabla \varphi$, respectively, where γ is any contour that encircles the core. Merons possess two distinct characteristics, corresponding to the combinations $(w, p) = \{(+1, -1/2), (-1, +1/2)\}$. Antimerons are counterparts to merons, possessing an opposing skyrmion number of $Q = +1/2$ with two distinct characteristics $(w, p) = \{(-1, -1/2), (+1, +1/2)\}$.

In continuous magnetic systems, merons and antimerons typically exist as pairs with opposite winding numbers ($w = +1$ and $w = -1$).^{7–13} The formation of such pairs allows their

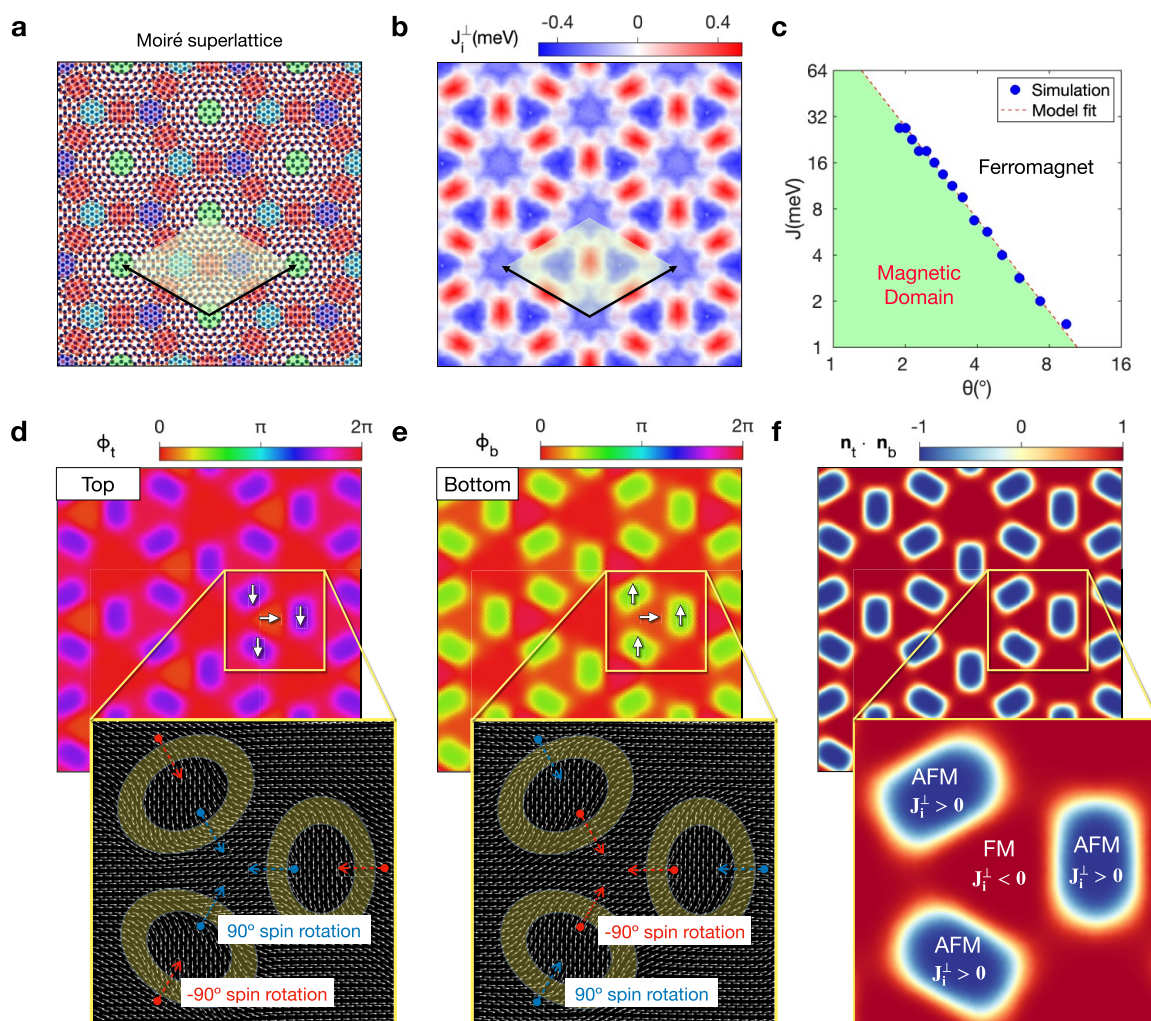


Figure 2. Emergence of AFM domain array. a: Moiré superlattice for a twist angle $\theta = 5.08^\circ$. The colored circles denote local stacking patterns including AA (green), AB (blue), BA (cyan), and monoclinic (red). The yellow rhombus and black arrows denote the unit cell and lattice vectors of the moiré superlattice, respectively. b: Modulation of the local interlayer exchange energy (J_i^\perp) computed for $\theta = 1.02^\circ$, with blue (red) color representing FM (AFM) coupling. c: Zero temperature magnetic phase diagram depicting FM phase (white) and magnetic domain phase (green), as a function of twist angle (θ) and intralayer exchange (J). The markers represent the phase boundary obtained from numerical simulations, while the dotted line indicates the fitting curve computed from an effective continuum model (see Supporting Information³⁸). d–f: Ground-state spin configuration in the magnetic domain phase for $J = 2$ meV and $\theta = 1.61^\circ$. d–e: The color scales denote the phase angles ($\phi_{t,b}$) of the normalized spin vectors $\mathbf{n}_{t,b} = (\cos \phi_{t,b}, \sin \phi_{t,b}, 0)$ in the top (d) and the bottom (e) layers, respectively. In the magnified images, the arrows denote the directions of \mathbf{n}_t and \mathbf{n}_b , and the yellow areas highlight the domain walls with 90° or -90° spin rotations. Here, “t” and “b” represent the top and bottom layers, respectively. f: The color scale denotes the relative orientation of the spin vectors between the two layers ($\mathbf{n}_t \cdot \mathbf{n}_b$), where red (blue) represents a parallel (antiparallel) alignment. The magnified image highlights the correspondence between the interlayer exchange and magnetic domain structure.

swirling spin textures to cancel out from the cores, resulting in localized spin configurations with finite energy. However, the mutual attraction between the cores renders the pairs inherently unstable, leading to pair annihilation during magnetization dynamics.⁴⁹ Consequently, in conventional untwisted magnetic systems, these magnetic textures are usually observed as transient states with a limited lifespan.^{7,8,13,16}

In this work, we discover that the merons and antimerons in twisted magnets can evade pair annihilation by forming a double Meron pair in two magnetic layers. To illustrate the emergence of such stable merons, we present a typical relaxation process of the magnetic state in Figure 3, which is obtained through the relaxation of a random initial configuration (see SI³⁸). In the intermediate magnetic state

(Figure 3a–b), we observe the spontaneous formation of four merons (M_{t1} , M_{t2} , M_{b1} , and M_{b2}) and four antimerons (\bar{M}_{t1} , \bar{M}_{t2} , \bar{M}_{b1} , and \bar{M}_{b2}) on the top and bottom layers. Upon subsequent relaxation, the intrapatch pairs, i.e., the Meron-antimeron pairs occupying the same AFM patch within the same layer such as $M_{t2}-\bar{M}_{t2}$ and $M_{b2}-\bar{M}_{b2}$, undergo pair annihilation due to the attractive interactions driven by the intralayer exchange interactions. However, the interpatch pairs, i.e., the Meron-antimeron pairs occupying different AFM patches within the same layer such as $M_{t1}-\bar{M}_{t1}$ and $M_{b1}-\bar{M}_{b1}$, remain robust against pair annihilation due to their mutual correlation facilitated by the interlayer coupling. As a result, the fully relaxed state (Figure 3c–d) accommodates only this correlated double Meron pair. Notably, our numerical analysis

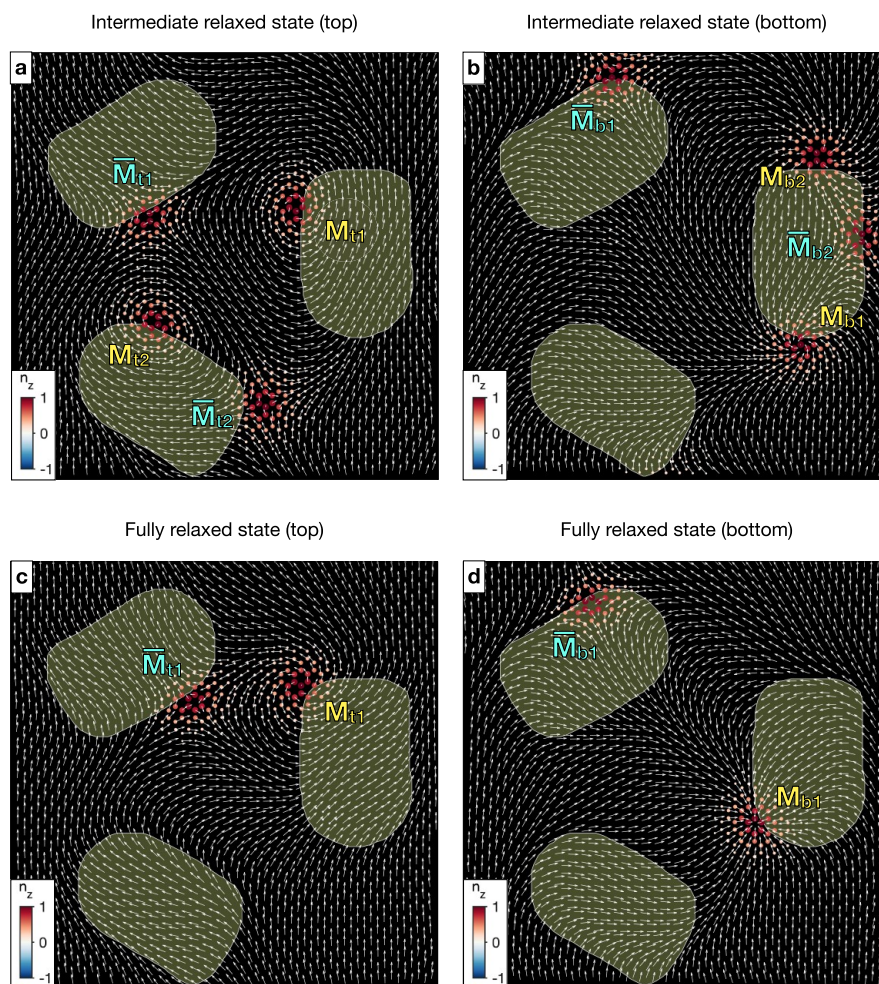


Figure 3. Snapshots depicting the relaxation process and the formation of stable meron–antimeron pairs. a–b: Intermediate state illustrating the spontaneous generation of merons (M_{t1} , M_{t2} , M_{b1} , and M_{b2}) and antimerons (\bar{M}_{t1} , \bar{M}_{t2} , \bar{M}_{b1} , and \bar{M}_{b2}). c–d: Fully relaxed state displaying stabilized Meron–antimeron pairs (M_{t1} – \bar{M}_{t1} , M_{b1} – \bar{M}_{b1}), with the annihilation of pairs M_{t2} – \bar{M}_{t2} and M_{b2} – \bar{M}_{b2} . Panels a, c and b, d represent the top and bottom layers, respectively, corresponding to a magnified area shown in Figure 2d–e. Arrows indicate in-plane components, while the color scale in the markers represents out-of-plane components. Marker sizes are adjusted for better visibility. Shaded areas indicate the AFM patches. The parameters $J = 2$ meV and $\theta = 1.61^\circ$ are utilized.

of these textures confirms their half-skyrmion-number characteristics (see SI³⁸).

We attribute the stabilization of the double Meron pair to the localization of their cores. During the relaxation process (Supporting Video 1), we observe that the cores shift exclusively along the boundaries of the AFM patches. This behavior arises from the bulk energy minimization condition: the requirement to minimize the interlayer exchange energy over the bulk region by maintaining the AFM domain configuration, i.e., antiparallel and parallel alignments inside and outside the AFM patches, as depicted in Figure 2f. Enforcing such a condition localizes the cores within their respective AFM patches by constraining their motions along the patch boundaries and prohibiting them from transferring to other patches. This localization mechanism preserves the interpatch pairs by ensuring the separation of their cores and protecting them against pair annihilation. However, the localization mechanism cannot preserve the intrapatch pairs, as their cores reside within the same patch (Supporting Video 2).

The localization mechanism of the Meron pair can be understood by considering the effective confining potential

arising from interlayer coupling (Figure 1c). The cores of merons in one layer (e.g., the top layer) experience an effective potential generated by the other layer (e.g., the bottom layer) through interlayer exchange coupling (Figure 4m). This potential reaches its minimum energy along the boundaries of the AFM patches due to the bulk energy minimization condition. Any displacement of the cores away from these boundaries results in increased energy relative to the minimum, creating potential wells along the AFM patch boundaries. These wells act as confining forces, effectively localizing the cores within them. Furthermore, the establishment of such potential wells requires the presence of two counterpart merons in the bottom layer to facilitate the bulk energy minimization condition. Consequently, the creation of four merons is required to protect the merons via the confining potential.

Based on our findings, we introduce a novel magnetic state dubbed the “Meron Quartet” (MQ) state, which consists of four merons, two for each layer, as depicted in Figure 4. This state exhibits two key characteristics: First, each layer contains two vortices with opposite winding numbers ($w = +1$ and $w = -1$), ensuring the total winding number cancels out. Second,

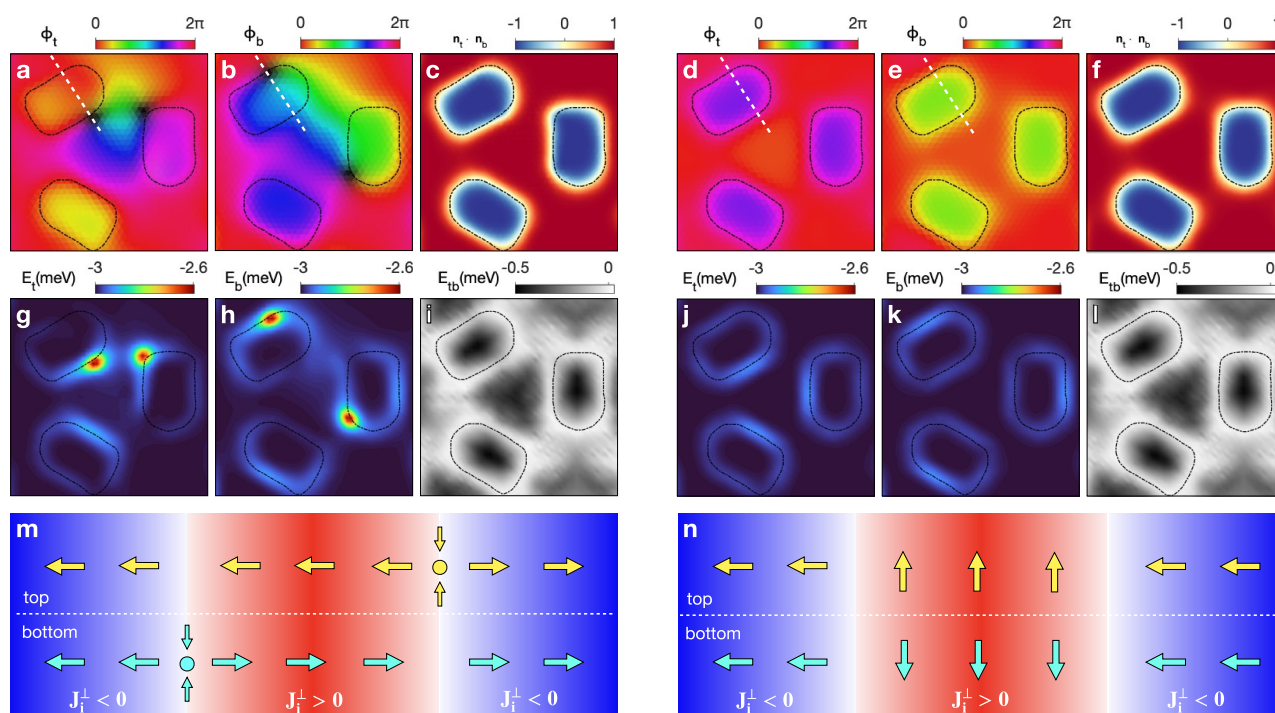


Figure 4. Comparison of Meron quartet (MQ) state to magnetic domain (MD) state. a–c/d–f: Spin configurations of the MQ (a–c) and MD (d–f) state, corresponding to Figure 3b,d and Figure 2d–f, respectively. a–b/d–e: Phase angles ($\phi_{t,b}$) of the normalized spin vectors ($\mathbf{n}_{t,b} = (\cos \phi_{t,b}, \sin \phi_{t,b}, 0)$) in the top (a/d) and bottom (b/e) layers. In a–b, the black color indicates out-of-plane polarization. c/f: Relative orientation ($\mathbf{n}_t \cdot \mathbf{n}_b$) between the top and bottom layers with red (blue) denoting parallel (antiparallel) alignment. g–i/j–l: Local magnetic energy maps corresponding to the spin configurations (a–c/d–f). g–h/j–k: Intralayer exchange energy plus single-ion anisotropy energy ($E_{t,b}$) in the top (g/j) and bottom (h/k) layers, respectively. i/l: Interlayer exchange energy (E_{tb}). In a–i, the dashed lines denote the boundaries of the AFM patches. m/n: Schematic illustration of the MQ (m) and MD (n) states across a single AFM patch, corresponding to the dotted lines shown in a–b and d–e, respectively. Red and blue colors depict the AFM patch region ($J_i^{\perp} > 0$) and FM coupling background ($J_i^{\perp} < 0$), respectively. Yellow and blue arrows represent spin orientations in the top and bottom layers, respectively.

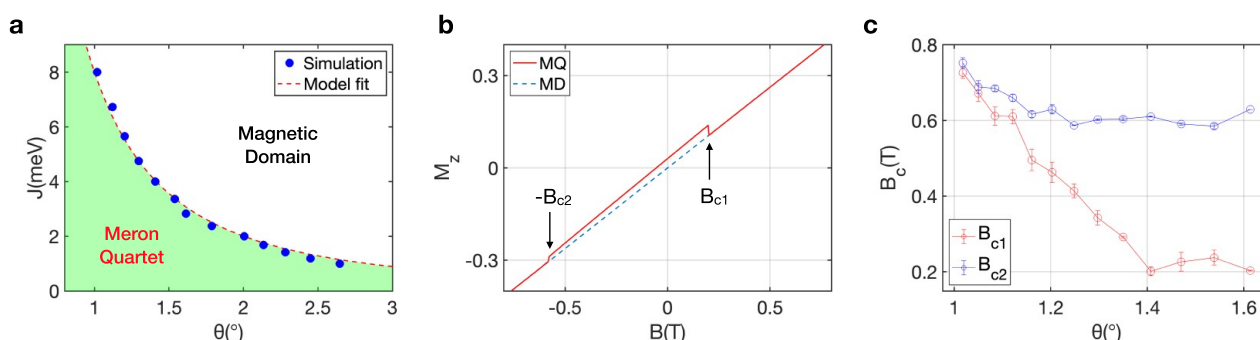


Figure 5. a: Magnetic phase diagram illustrating the Meron quartet phase (green) and the magnetic domain phase (white), as a function of twist angle (θ) and intralayer exchange (J). The markers represent the phase boundary determined through numerical simulations, while the dashed line represents the phenomenological fitting curve $\theta_{c2} = \sqrt{J_{c2}/J}$, where the fitting parameter J_{c2} is found to be 8 meV. b: Out-of-plane net magnetization ($M_z = 1/N \sum_{i=t,b} \sum_i n_{i,z}^l$) as a function of an external magnetic field in the out-of-plane direction (B), with the solid and dashed lines corresponding to the MQ and MD states, as depicted in Figure 4a–c and d–f, respectively. The arrows mark the critical field strengths (B_{c1} and B_{c2}) that signify the degradation of the MQ state to the MD state, as shown by merging of the two curves at B_{c1} and $-B_{c2}$. c: Evolution of B_{c1} and B_{c2} with the twist angle (θ). Error bars denote standard errors from different samples. The parameter $J = 2$ meV is utilized.

each occupied AFM patch harbors two vortices with the same winding numbers ($w = +1$ or $w = -1$) in both the top and bottom layers. These specific arrangements enable the MQ state to realize stable Meron pairs through the implementation of the confining potential. Furthermore, the MQ state minimizes the interlayer exchange energy over the bulk region (Figure 4c,i), as observed in the ground MD state (Figure 4f,l). The distinction between the MQ and MD states lies solely in the localized core energy (Figure 4g–h vs j–k). As a result, the

MQ state exhibits a low magnetic energy of -3.064 meV per spin, comparable to the energy of the ground MD state (-3.071 meV), despite its intricate spin textures arising from the presence of merons (Figure 4a–b). In other words, the MQ state naturally accommodates the stable correlated pairs of merons, i.e., the Meron quartet, while satisfying the bulk energy minimization condition (Figure 4m), similar to the ground MD state (Figure 4n).

We observe that the MQ state acquires metastability in the small twist angle regime (green area in Figure 5a). This phenomenon is attributed to the enhancement of the confining potential in such a regime. To elucidate this, we consider the transition from the MQ state to the MD state. This transition necessitates mutual attraction of the Meron cores. However, such attraction leads to an inevitable increase in the interlayer exchange energy, as it disrupts the bulk energy minimization condition, as illustrated in Figure 4c,i. We estimate this energy increase as $\Delta E_{\text{tb}} \sim J_{\perp}^{\text{FM}} \frac{dL}{a^2}$, where J_{\perp}^{FM} represents the FM interlayer exchange near an AFM patch, and d signifies the displacement of a core from its equilibrium position due to the attraction. The term $\frac{dL}{a^2} \sim \frac{d}{a\theta}$ corresponds to the number of spins that undergo unfavorable ordering for the interlayer exchange, which increases as the twist angle θ decreases. Consequently, this energy cost escalates as the twist angle θ decreases, creating a substantial energy barrier for the transition to the MD state, which corresponds to the confining potential mentioned before.

This high energy barrier surpasses the attractive force between merons and analogues, stabilizing the MQ state. The attractive force is mediated by the intralayer exchange interaction energy between a meron and an antimeron within the same layer. This energy is akin to the Coulomb energy between a vortex and an antivortex in the XY model, denoted as $E_C \sim J \ln(R/a)$,⁴⁹ where $R \sim a/\theta$ represents the distance between the cores. The attraction of the cores by a displacement of d can potentially reduce the Coulomb energy by $\Delta E_C \sim -Jd/R \sim -Jd\theta/a$. However, this energy reduction ΔE_C is surpassed by the energy increase ΔE_{tb} in the small twist angle regime ($\theta < \theta_{c2} \sim \sqrt{J_{\perp}^{\text{FM}}/J}$). As a result, attraction of the cores is effectively prohibited in such a regime, leading to stabilization of the MQ state. We find that this phenomenon is evident in the phase diagram, which exhibits a consistent relationship $\theta_{c2} = \sqrt{J_{c2}/J}$ (dashed line in Figure 5a), where J_{c2} is a fitting parameter proportional to J_{\perp}^{FM} .

The high energy barrier also indicates the enhanced stability of the MQ state against external perturbations, such as external magnetic fields, in the small twist angle regime. To further illustrate this stability, we incorporate the Zeeman term:

$$H_{\text{Zeeman}} = -g\mu_B B \sum_{l=t,b} \sum_i S_{i,z}^l \quad (3)$$

where B represents an external magnetic field applied in the out-of-plane direction. Through the systematic examination of the behavior of the MQ state under the influence of the Zeeman term (see SI³⁸), we identify the critical field strength for the destruction of the MQ state, as illustrated in Figure 5b. The critical field strength differs depending on the relative orientation of the applied field with respect to the polarity of the meron and antimeron cores, with the antiparallel field exhibiting a much higher critical field strength (B_{c2}) compared to the parallel field (B_{c1}). Nevertheless, both critical field strengths are significantly enhanced as the twist angle decreases (Figure 5c). This corroborates the enhanced stability of the MQ state in the small twist angle regime.

In principle, the detailed profile of the interlayer exchange coupling can impact the formation of MQ states. Our investigation into smoothed variations of the interlayer coupling consistently demonstrates the formation of MQ

states as long as the coexistence of AFM-FM interlayer coupling is maintained. Nevertheless, the specific coupling pattern plays a crucial role in determining the configurations of MQ states and the critical twist angle for their emergence. See SI³⁸ for further details.

In certain materials, magnetic dipole–dipole interactions play a dominant role in attaining the easy-plane magnetic behavior essential for the emergence of merons. Our investigation demonstrates that the inclusion of the dipole–dipole interactions leads to an expansion of the formation of MQ states, even into the easy-axis single-ion anisotropy regime (i.e., $A < 0$), whereas overall easy-plane anisotropy is maintained owing to these interactions. This observation suggests the potential applicability of the theoretical findings in this work to materials exhibiting these characteristics, such as CrCl₃.¹⁵ See SI³⁸ for further details.

We discover that the twisted magnet can realize stable merons in diverse forms with a different total skyrmion number ($Q_{\text{tot}} = 0, \pm 1, \pm 2$) and distinct combinations of merons and antimerons between two magnetic layers in addition to the specific configuration shown in Figure 4a–c. Due to the condition of the vanishing of the total winding number, two vortices consisting of each interpatch pair must exhibit opposite winding numbers $w = +1$ and $w = -1$, respectively. However, the cores have the flexibility to possess their own polarity, which can be either $p = -1/2$ or $p = +1/2$. This gives rise to four potential configurations for each pair: (i) M–M, (ii) \bar{M} –M, (iii) M– \bar{M} , and (iv) \bar{M} – \bar{M} . Furthermore, these configurations can independently occur in the top and bottom layers, resulting in a total of 16 potential configurations for the MQ state, with distinct numbers of merons and antimerons in each layer. Our investigation employing general random initial configurations, our investigation confirms the emergence of such diverse configurations. Furthermore, we have verified the degenerate nature of these configurations in twist angle variations. (see SI³⁸). This observation highlights the flexibility in achieving merons and antimerons in the twisted magnet, setting it apart from conventional magnetic systems, which typically have fixed skyrmion numbers.^{1,13}

We have shown that the AFM domain array induced by the twist provides a favorable environment for hosting stable merons. Once these topological defects form, their destruction is impeded due to the constraints imposed by the bulk energy minimization condition. Moreover, our theory suggests the feasibility of realizing such stable moieties and their enhanced robustness in the small twist angle regime.

We propose our theory can be applied to CrCl₃, which exhibits two essential factors for hosting the Meron quartet: easy-plane magnetic anisotropy¹⁵ and stacking-dependent interlayer magnetism.²¹ Notably, merons have been observed in monolayer CrCl₃.^{15,16} In this context, twist engineering offers an effective approach to realizing the Meron quartet. Another potential application lies in CrI₃, where the modification of its intrinsic easy-axis magnetic anisotropy to easy-plane anisotropy can be achieved through experimental control, such as gate-voltage tuning.^{44–48}

For experimental observations, we propose utilizing scanning magnetometry techniques with nitrogen-vacancy centers,²⁹ as well as Lorentz transmission electron microscopy⁵⁰ and magnetic transmission soft X-ray microscopy,¹³ to directly observe Meron pairs ranging in size from 80 to 20 nm at different twist angles ($\theta = 0.5^\circ$ to 2°). Indirect measurements can involve detecting anomalous kinks in the magnet-

ization curve, which can serve as an indication of the presence of merons. Techniques such as the magneto-optical Kerr effect, commonly employed in the study of 2D vdW magnets,^{30,31} can offer valuable insights for such indirect measurements.

Future research should consider incorporating various magnetic interactions present in vdW magnets that were overlooked in our current model, such as exchange anisotropy, interactions beyond nearest neighbors,¹⁶ the Dzyaloshinskii–Moriya interaction, and magnetic dipole–dipole interactions.¹⁵ An important research question to explore is how these additional interactions impact the stabilization of the Meron quartet and their behavior in vdW magnets.

We highlight that the discovery and realization of merons in 2D vdW magnets via twist open a unique avenue for investigating their fascinating properties with remarkable flexibility, through either external stimuli^{35,36} or the creation of heterostructures.³⁷ This significant breakthrough not only deepens our understanding of these fractionalized topological spin textures in magnets but also holds great promise for future technological advancements.

■ ASSOCIATED CONTENT

SI Supporting Information

The Supporting Information is available free of charge at <https://pubs.acs.org/doi/10.1021/acs.nanolett.3c03246>.

Interlayer Heisenberg exchange coupling map, spin configuration relaxation methods, expansion of spin configuration data, classification of Meron quartet states, determination of phase boundaries, and impact of dipole–dipole interactions (PDF)

Relaxation process (AVI)

Localization mechanism (AVI)

■ AUTHOR INFORMATION

Corresponding Authors

Kyoung-Min Kim – Center for Theoretical Physics of Complex Systems, Institute for Basic Science, Daejeon 34126, Republic of Korea; orcid.org/0000-0003-2468-3152;
Email: kmkim@ibs.re.kr

Se Kwon Kim – Department of Physics, Korea Advanced Institute of Science and Technology, Daejeon 34141, Republic of Korea; orcid.org/0000-0002-2849-9718;
Email: sekwonkim@kaist.ac.kr

Authors

Gyungchoon Go – Department of Physics, Korea Advanced Institute of Science and Technology, Daejeon 34141, Republic of Korea

Moon Jip Park – Department of Physics, Hanyang University, Seoul 04763, Republic of Korea

Complete contact information is available at:

<https://pubs.acs.org/doi/10.1021/acs.nanolett.3c03246>

Notes

The authors declare no competing financial interest.

■ ACKNOWLEDGMENTS

K.K. acknowledges support from the Institute for Basic Science in the Republic of Korea under the project IBS-R024-D1. G.G. was supported by the National Research Foundation of Korea (NRF-2022R1C1C2006578). M.J.P. was supported by the National Research Foundation of Korea (NRF) grant funded

by the Korea government (MSIT) (RS-2023-00252085, RS-2023-00218998). Lastly, S.K.K. was supported by Brain Pool Plus Program through the National Research Foundation of Korea funded by the Ministry of Science and ICT (2020H1D3A2A03099291) and National Research Foundation of Korea funded by the Korea Government via the SRC Center for Quantum Coherence in Condensed Matter (RS-2023-00207732).

■ REFERENCES

- (1) Nagaosa, N.; Tokura, Y. Topological properties and dynamics of magnetic skyrmions. *Nat. Nanotechnol.* **2013**, *8*, 899–911.
- (2) Shinjo, T.; Okuno, T.; Hassdorf, R.; Shigeto, K.; Ono, T. Magnetic Vortex Core Observation in Circular Dots of Permalloy. *Science* **2000**, *289*, 930–932.
- (3) Phatak, C.; Petford-Long, A. K.; Heinonen, O. Direct Observation of Unconventional Topological Spin Structure in Coupled Magnetic Discs. *Phys. Rev. Lett.* **2012**, *108*, No. 067205.
- (4) Wintz, S.; Bunce, C.; Neudert, A.; Körner, M.; Strache, T.; Buhl, M.; Erbe, A.; Gemming, S.; Raabe, J.; Quitmann, C.; Fassbender, J. Topology and Origin of Effective Spin Meron Pairs in Ferromagnetic Multilayer Elements. *Phys. Rev. Lett.* **2013**, *110*, No. 177201.
- (5) Tan, A.; Li, J.; Scholl, A.; Arenholz, E.; Young, A. T.; Li, Q.; Hwang, C.; Qiu, Z. Q. Topology of spin Meron pairs in coupled Ni/Fe/Co/Cu(001) disks. *Phys. Rev. B* **2016**, *94*, No. 014433.
- (6) Shigeto, K.; Okuno, T.; Mibu, K.; Shinjo, T.; Ono, T. Magnetic force microscopy observation of antivortex core with perpendicular magnetization in patterned thin film of permalloy. *Appl. Phys. Lett.* **2002**, *80*, 4190–4192.
- (7) Fu, X.; Pollard, S. D.; Chen, B.; Yoo, B.-K.; Yang, H.; Zhu, Y. Optical manipulation of magnetic vortices visualized in situ by Lorentz electron microscopy. *Sci. Adv.* **2018**, *4*, No. eaat3077.
- (8) Van Waeyenberge, B.; Puzic, A.; Stoll, H.; Chou, K. W.; Tylliszczak, T.; Hertel, R.; Fähnle, M.; Brückl, H.; Rott, K.; Reiss, G.; Neudecker, I.; Weiss, D.; Back, C. H.; Schütz, G. Magnetic vortex core reversal by excitation with short bursts of an alternating field. *Nature* **2006**, *444*, 461–464.
- (9) Ruotolo, A.; Cros, V.; Georges, B.; Dussaux, A.; Grollier, J.; Deranlot, C.; Guillemet, R.; Bouzehouane, K.; Fusil, S.; Fert, A. Phase-locking of magnetic vortices mediated by antivortices. *Nat. Nanotechnol.* **2009**, *4*, 528–532.
- (10) Roy, P. E.; Lee, J. H.; Trypiniotis, T.; Anderson, D.; Jones, G. A. C.; Tse, D.; Barnes, C. H. W. Antivortex domain walls observed in permalloy rings via magnetic force microscopy. *Phys. Rev. B* **2009**, *79*, No. 060407.
- (11) Chmiel, F. P.; Waterfield Price, N.; Johnson, R. D.; Lamirand, A. D.; Schad, J.; van der Laan, G.; Harris, D. T.; Irwin, J.; Rzechowski, M. S.; Eom, C.-B.; Radaelli, P. G. Observation of magnetic vortex pairs at room temperature in a planar α -Fe₂O₃/Co heterostructure. *Nat. Mater.* **2018**, *17*, 581–585.
- (12) Yu, X. Z.; Koshibae, W.; Tokunaga, Y.; Shibata, K.; Taguchi, Y.; Nagaosa, N.; Tokura, Y. Transformation between Meron and skyrmion topological spin textures in a chiral magnet. *Nature* **2018**, *564*, 95–98.
- (13) Gao, N.; Je, S.-G.; Im, M.-Y.; Choi, J. W.; Yang, M.; Li, Q.; Wang, T. Y.; Lee, S.; Han, H.-S.; Lee, K.-S.; Chao, W.; Hwang, C.; Li, J.; Qiu, Z. Q. Creation and annihilation of topological Meron pairs in in-plane magnetized films. *Nat. Commun.* **2019**, *10*, No. 5603.
- (14) Bedoya-Pinto, A.; Ji, J.-R.; Pandeya, A. K.; Gargiani, P.; Valvidares, M.; Sessi, P.; Taylor, J. M.; Radu, F.; Chang, K.; Parkin, S. P. Intrinsic 2D-XY ferromagnetism in a van der Waals monolayer. *Science* **2021**, *374*, 616–620.
- (15) Lu, X.; Fei, R.; Zhu, L.; Yang, L. Meron-like topological spin defects in monolayer CrCl₃. *Nat. Commun.* **2020**, *11*, No. 4724.
- (16) Augustin, M.; Jenkins, S.; Evans, R. F. L.; Novoselov, K. S.; Santos, E. J. G. Properties and dynamics of Meron topological spin textures in the two-dimensional magnet CrCl₃. *Nat. Commun.* **2021**, *12*, 185.

- (17) Tong, Q.; Liu, F.; Xiao, J.; Yao, W. Skyrmions in the Moiré of van der Waals 2D Magnets. *Nano Lett.* **2018**, *18*, 7194–7199.
- (18) Hejazi, K.; Luo, Z.-X.; Balents, L. Heterobilayer moiré magnets: Moiré skyrmions and commensurate-incommensurate transitions. *Phys. Rev. B* **2021**, *104*, No. L100406.
- (19) Akram, M.; Erten, O. Skyrmions in twisted van der Waals magnets. *Phys. Rev. B* **2021**, *103*, No. L140406.
- (20) Xiao, F.; Chen, K.; Tong, Q. Magnetization textures in twisted bilayer CrX_3 ($X = \text{Br}, \text{I}$). *Phys. Rev. Research* **2021**, *3*, No. 013027.
- (21) Akram, M.; LaBollita, H.; Dey, D.; Kapeghian, J.; Erten, O.; Botana, A. S. Moiré Skyrmions and Chiral Magnetic Phases in Twisted CrX_3 ($X = \text{I}, \text{Br}$, and Cl) Bilayers. *Nano Lett.* **2021**, *21*, 6633–6639.
- (22) Ghader, D.; Jabakhanji, B.; Stroppa, A. Whirling interlayer fields as a source of stable topological order in moiré CrI_3 . *Commun. Phys.* **2022**, *5*, 192.
- (23) Zheng, F. Magnetic Skyrmion Lattices in a Novel 2D-Twisted Bilayer Magnet. *Adv. Funct. Mater.* **2023**, *33*, No. 2206923.
- (24) Kim, K.-M.; Kiem, D. H.; Bednik, G.; Han, M. J.; Park, M. J. Ab Initio Spin Hamiltonian and Topological Noncentrosymmetric Magnetism in Twisted Bilayer CrI_3 . *Nano Lett.* **2023**, *23*, 6088–6094.
- (25) Fumega, A. O.; Lado, J. L. Moiré-driven multiferroic order in twisted CrCl_3 , CrBr_3 and CrI_3 bilayers. *2D Materials* **2023**, *10*, No. 025026.
- (26) Berezinsky, V. L. Destruction of long range order in one-dimensional and two-dimensional systems having a continuous symmetry group. I. Classical systems. *Sov. Phys. JETP* **1971**, *32*, 493–500.
- (27) Kosterlitz, J. M.; Thouless, D. J. Ordering, metastability and phase transitions in two-dimensional systems. *J. Phys. C* **1973**, *6*, 1181–1203.
- (28) Burch, K. S.; Mandrus, D.; Park, J.-G. Magnetism in two-dimensional van der Waals materials. *Nature* **2018**, *563*, 47–52.
- (29) Song, T.; Sun, Q.-C.; Anderson, E.; Wang, C.; Qian, J.; Taniguchi, T.; Watanabe, K.; McGuire, M. A.; Stöhr, R.; Xiao, D.; Cao, T.; Wrachtrup, J.; Xu, X. Direct visualization of magnetic domains and moiré magnetism in twisted 2D magnets. *Science* **2021**, *374*, 1140–1144.
- (30) Xu, Y.; Ray, A.; Shao, Y.-T.; Jiang, S.; Lee, K.; Weber, D.; Goldberger, J. E.; Watanabe, K.; Taniguchi, T.; Muller, D. A.; Mak, K. F.; Shan, J. Coexisting ferromagnetic-antiferromagnetic state in twisted bilayer CrI_3 . *Nat. Nanotechnol.* **2022**, *17*, 143–147.
- (31) Xie, H.; Luo, X.; Ye, G.; Ye, Z.; Ge, H.; Sung, S. H.; Rennich, E.; Yan, S.; Fu, Y.; Tian, S.; Lei, H.; Hovden, R.; Sun, K.; He, R.; Zhao, L. Twist engineering of the two-dimensional magnetism in double bilayer chromium triiodide homostructures. *Nat. Phys.* **2022**, *18*, 30–36.
- (32) Xie, H.; Luo, X.; Ye, Z.; Sun, Z.; Ye, G.; Sung, S. H.; Ge, H.; Yan, S.; Fu, Y.; Tian, S.; Lei, H.; Sun, K.; Hovden, R.; He, R.; Zhao, L. Evidence of non-collinear spin texture in magnetic moiré superlattices. *Nat. Phys.* **2023**, *19*, 1150–1155.
- (33) Hejazi, K.; Luo, Z.-X.; Balents, L. Noncollinear phases in moiré magnets. *Proc. Natl. Acad. Sci. U.S.A.* **2020**, *117*, 10721–10726.
- (34) Kim, K.-M.; Park, M. J. Controllable magnetic domains in twisted trilayer magnets. *Phys. Rev. B* **2023**, *108*, No. L100401.
- (35) Wang, Z.; et al. Electric-field control of magnetism in a few-layered van der Waals ferromagnetic semiconductor. *Nat. Nanotechnol.* **2018**, *13*, 554–559.
- (36) Jiang, S.; Li, L.; Wang, Z.; Mak, K. F.; Shan, J. Controlling magnetism in 2D CrI_3 by electrostatic doping. *Nat. Nanotechnol.* **2018**, *13*, 549–553.
- (37) Gibertini, M.; Koperski, M.; Morpurgo, A. F.; Novoselov, K. S. Magnetic 2D materials and heterostructures. *Nat. Nanotechnol.* **2019**, *14*, 408–419.
- (38) See Supporting Information.
- (39) Sivadas, N.; Okamoto, S.; Xu, X.; Fennie, C. J.; Xiao, D. Stacking-Dependent Magnetism in Bilayer CrI_3 . *Nano Lett.* **2018**, *18*, 7658–7664.
- (40) Jang, S. W.; Jeong, M. Y.; Yoon, H.; Ryee, S.; Han, M. J. Microscopic understanding of magnetic interactions in bilayer CrI_3 . *Phys. Rev. Mater.* **2019**, *3*, No. 031001.
- (41) Song, T.; et al. Switching 2D magnetic states via pressure tuning of layer stacking. *Nat. Mater.* **2019**, *18*, 1298–1302.
- (42) Li, T.; Jiang, S.; Sivadas, N.; Wang, Z.; Xu, Y.; Weber, D.; Goldberger, J. E.; Watanabe, K.; Taniguchi, T.; Fennie, C. J.; Fai Mak, K.; Shan, J. Pressure-controlled interlayer magnetism in atomically thin CrI_3 . *Nat. Mater.* **2019**, *18*, 1303–1308.
- (43) Chen, W.; Sun, Z.; Wang, Z.; Gu, L.; Xu, X.; Wu, S.; Gao, C. Direct observation of van der Waals stacking-dependent interlayer magnetism. *Science* **2019**, *366*, 983–987.
- (44) Webster, L.; Yan, J.-A. Strain-tunable magnetic anisotropy in monolayer CrCl_3 , CrBr_3 , and CrI_3 . *Phys. Rev. B* **2018**, *98*, No. 144411.
- (45) Kim, J.; Kim, K.-W.; Kim, B.; Kang, C.-J.; Shin, D.; Lee, S.-H.; Min, B.-C.; Park, N. Exploitable Magnetic Anisotropy of the Two-Dimensional Magnet CrI_3 . *Nano Lett.* **2020**, *20*, 929–935.
- (46) Xu, Q.-F.; Xie, W.-Q.; Lu, Z.-W.; Zhao, Y.-J. Theoretical study of enhanced ferromagnetism and tunable magnetic anisotropy of monolayer CrI_3 by surface adsorption. *Phys. Lett. A* **2020**, *384*, No. 126754.
- (47) Tang, C.; Zhang, L.; Du, A. Tunable magnetic anisotropy in 2D magnets via molecular adsorption. *J. Mater. Chem. C* **2020**, *8*, 14948–14953.
- (48) Tang, M.; et al. Continuous manipulation of magnetic anisotropy in a van der Waals ferromagnet via electrical gating. *Nat. Electron.* **2022**, *6*, 28–36.
- (49) Hubert, A.; Schäfer, R. *Magnetic Domains*; Springer: Berlin, 1998.
- (50) Ding, B.; Li, Z.; Xu, G.; Li, H.; Hou, Z.; Liu, E.; Xi, X.; Xu, F.; Yao, Y.; Wang, W. Observation of Magnetic Skyrmion Bubbles in a van der Waals Ferromagnet Fe_3GeTe_2 . *Nano Lett.* **2020**, *20*, 868–873.